Processing and analysis of HF radar measurements of currents and sea states in the Iroise and Celtic Seas

MERIFIC Deliverable 3. .!

Actimar :

C. Taillandier
H. Pineau
N. Thomas

Ifremer :

C. Maisondieu

Plymouth University :

G. Lopez
D. Conley

MERiFIC was selected under the European Cross-Border Cooperation Programme INTERREG IV A France (Channel) – England, co-funded by the ERDF.

The sole responsibility for the content of this report lies with the authors. It does not represent the opinion of the European Communities. The European Commission is not responsible for any use that may be made of the information contained therein.

Summary

Introduction ..... "
" Surface current measurement using #ER$ HF radars data ..... "
.1 Development of the operational DF method for the WERA HF radars data .....
.1.1 The S RT RADIAL Processing tool 3

3 Sea%states measurement from #ER$ HF radars& 'rocessing and analysis .....3(
3.1 Significant wave height (Hs) measurement using WERA HF radars 35
3.1.1 Classical empirical method 35
3.1.1.1 Description 35
3.1.1. Quality control of radars measurement 35
3.1.1.3 Calibration of the empirical algorithm for the Iroise sea 38
3.1. The empirical method adapted to the configuration of the Iroise Sea 41
3.1. .1 Description 41
3.1. . Quality control of the radar measurements 4
3.1. .3 Discussions on the results of the modified empirical method 44
3.1. .4 Processing of the Plymouth University data sets 47
3.1.3 The empirical method calibrated for the Celtic Sea 49
3.1.3.1 Description 49
3.1.3. Quality control of the radar measurements 50
3.1.3.3 Discussion on the results of the modified empirical method 5
3.1.4 Feasibility and validation study of a Barrick's Equation inversion method 53
3.1.4.1 Description 53
3.1.4. Nonlinear inversion based on Hisaki formulation.....Error) *oo+mar+ not defined.
3.1.4.3 Comparison of the linearized and empirical methods....Error) *oo+mar+ not defined.
3. Statistics of significant wave heights measured by HF radars in the Iroise Sea 60
3. .1 Data pre-processing 60
3. .1.1 HF radar sea-states data 60
3. .1. Masking 61
3. . Sea-states statistics in the Iroise Sea 63
3. . .1 Mapping of the results 63
3. . . Detailed analysis at different locations 67
3.3 Statistics of significant wave heights measured by HF radars in the Celtic Sea. 68
3.3.1 Data pre-processing 68
3.3.1.1 HF radar sea-states data 68
3.3.1. Masking 69
3.3. Sea-states statistics in the Celtic Sea 70
3.3. .1 Mapping of the results 70
3.3. . Detailed analysis at different locations 73
! Conclusions .....,-

ist of Figures

Figure 1 : S RT RADIAL Azimutal processing chain....4
Figure : Fromveur area and reference measurement point (red dot)....4
Figure 3 : Time series for the methods BF (blue) and DF (green), East-West component. ..5
Figure 4 : Scatter plot and Q-Q plot for both methods BF and DF, East-West Component 5
Figure 5 : Time series for the methods BF (blue) and DF (green), North - South component. 6
Figure 6 : Scatter plot and Q-Q plot for both methods BF and DF, North – South Component6
Figure 7 : Time series for the methods BF (blue) and DF (green), Norm of the total vector.7
Figure 8 : Scatter plot and Q-Q plot for both methods BF and DF, Norm of the total vector 7
Figure 9 : Location of the ADCP surveys over the Iroise Sea 8
Figure 10 : Time series of ADCP measured (red) and BF (blue) and DF (green) methods, East-West component 9
Figure 11 : Scatter plot and Q-Q plot for both methods BF (blue) and DF (green) as functions of ADCP measurement, East-West Component 10
Figure 1 : Scatter plot and Q-Q plot comparison of BF and DF methods, East-West Component....10
Figure 13 : Time series of ADCP measured (red) and BF (blue) and DF (green) methods, North - South component 11
Figure 14 : Scatter plot and Q-Q plot for both methods BF (blue) and DF (green) as functions of ADCP measurement, North - South Component 11
Figure 15 : Scatter plot and Q-Q plot comparison of BF and DF methods, North - South Component....1
Figure 16 : Time series of ADCP measured (red) and BF (blue) and DF (green) methods, Norm of the total vector 1
Figure 17 : Scatter plot and Q-Q plot for both methods BF (blue) and DF (green) as functions of ADCP measurement, Norm of the total vector 13
Figure 18 : Scatter plot and Q-Q plot comparison of BF and DF methods, Norm of the total vector 13
Figure 19 : Time series of ADCP measured (red) and BF (blue) and DF (green) methods, East-West component 14
Figure 0 : Scatter plot and Q-Q plot for both methods BF (blue) and DF (green) as functions of ADCP measurement, East-West Component 14
Figure 1 : Scatter plot and Q-Q plot comparison of BF and DF methods, East-West Component....15
Figure : Time series of ADCP measured (red) and BF (blue) and DF (green) methods, North - South component 15
Figure 3 : Scatter plot and Q-Q plot for both methods BF (blue) and DF (green) as functions of ADCP measurement, North - South Component 16
Figure 4 : Scatter plot and Q-Q plot comparison of BF and DF methods, North - South Component....16
Figure 5 : Time series of ADCP measured (red) and BF (blue) and DF (green) methods, Norm of the total vector 17
Figure 6 : Scatter plot and Q-Q plot for both methods BF (blue) and DF (green) as functions of ADCP measurement, Norm of the total vector 17
Figure 7 : Scatter plot and Q-Q plot comparison of BF and DF methods, Norm of the total vector 18

Figure 8 : space coverage and rate of occurrence of surface current measurement over the period 07/ 006 - 08/ 011 19
Figure 9 : mean surface current velocity amplitudes over the period 07/ 006 - 08/ 011 0
Figure 30 : Median value of surface current velocity amplitudes over the period 07/ 006 - 08/ 011 0
Figure 31 : 99% quantile of surface current velocity amplitudes over the period 07/ 006 - 08/ 011 1
Figure 3 : Probability of occurrence of velocities higher than 0. 5 m/s over the period 07/ 006 - 08/ 011 1
Figure 33 : Probability of occurrence of velocities higher than 0.5 m/s over the period 07/ 006 - 08/ 011 .....
Figure 34 : Probability of occurrence of velocities higher than 0.75 m/s over the period 07/ 006 - 08/ 011 .....
Figure 35 : Probability of occurrence of velocities higher than 1 m/s over the period 07/ 006 - 08/ 011 3
Figure 36 : Probability of occurrence of velocities higher than 1.5 m/s over the period 07/ 006 - 08/ 011 3
Figure 37 : Frequency of occurrence of directions (polar histograms) superimposed with mean velocity amplitude of surface currents over 07/ 006 - 08/ 011 4
Figure 38 : Frequency of occurrence of directions (polar histograms) superimposed with mean velocity amplitude of surface currents around Ushant Island over 07/ 006 - 08/ 011. 4
Figure 39 : Surface currents compass rose around Ushant Island, 07/ 006 - 08/ 011 5
Figure 40 : Statistics in the Fromveur strait (Point N°11) over the period 07/ 006 - 08/ 011. Velocity amplitudes histogram (upper left), directions histogram (upper right), currents compass rose (lower left), currents compass rose for currents > 0.5 m/s (lower right)..... 6
Figure 41 : Statistics in the North-west of Ushant island (Point N°5) over the period 07/ 006 - 08/ 011. Velocity amplitudes histogram (upper left), directions histogram (upper right), currents compass rose (lower left), currents compass rose for currents > 0.5 m/s (lower right)..... 7
Figure 4 : measured currents for tides with tidal coefficient 45..... 8
Figure 43 : Current compasses for tides with a tidal coefficient of 45..... 9
Figure 44 : Current compasses for tides with a tidal coefficient of 70.....30
Figure 45 : Current compasses for tides with a tidal coefficient of 95.....31
Figure 46 : Max of current velocity amplitude for flood (left) and ebb (right) for a tidal coefficient of 45 3
Figure 47 : Max of current velocity amplitude for flood (left) and ebb (right) for a tidal coefficient of 95 3
Figure 48 : Maps of the differences of the annual mean current velocity obtained using DF and BF methods 33
Figure 49 : BF method, statistics in the Fromveur strait (point N°11) : velocity compass and histogram. 33
Figure 50 : DF method, statistics in the Fromveur strait (point N°11) : velocity compass and histogram. 34
Figure 51 : Location of wave buoys used for the analysis.....35
Figure 5 : comparison of HF radar and 0 911 wave buoy Hs data - ctober 009 to July 010. 36
Figure 53 : comparison of HF radar and 0 90 wave buoy Hs data - ctober 009 to July 010. 37

Figure 54 : Calibration curves for the Hs measurement empirical algorithm. 38
Figure 55 : Comparison between radar Hs and 0 911 wave buoy Hs before calibration - December 009.....40
Figure 56 : Comparison between radar Hs and 0 911 wave buoy Hs after calibration - December 009.....41
Figure 57 : comparison of HF radar and 0 911 wave buoy Hs data - ctober 009 to July 010 - Modified empirical method.....4
Figure 58 : comparison of HF radar and 0 90 wave buoy Hs data - ctober 009 to July 010 - Modified empirical method.....43
Figure 59 : Comparison of Hs measured by the wave buoy 0 911 and estimated from radar data using the modified empirical method - December 009 44
Figure 60 : Comparison between Norgas wave model and buoy 0 90 " uessant Large"...45
Figure 61 : Norgas model significant wave height compared with radar measurement using classical and modified empirical method at the location " uessant Large".....46
Figure 6 : Norgas model significant wave height compared with radar measurement using the classical empirical method at the location " uessant Large". 46
Figure 63 : Norgas model significant wave height compared with radar measurement using the modified empirical method at the location " uessant Large". 47
Figure 64 : Location of the PU HF Radars and reference wave buoy 47
Figure 65 : Map of Significant wave height measured by the PU HF radars 48
Figure 66 : Comparison of the classical (left) and modified (right) empirical methods with wave buoy data - PU Radar data.....48
Figure 67: Location of the wave buoy used both for calibration and validation of the empirical method. The coordinates of the wave buoy are 50.34 N, -05.6057W.....49
Figure 68 : Calibration curves for the Hs measurement empirical algorithm 50
Figure 69: Comparison between radar Hs and Wave Hub buoy before calibration – March 01 to December 01 51
Figure 70: Comparison between radar Hs and Wave Hub buoy after calibration – March 01 to December 01 5
Figure 71: Comparison of HF radar and wave buoy Hs data – May 01 – Modified empirical method. 53
Figure 7 : Wave directional spectrum obtained from nonlinear inversion of the radar data - "Pierres Noires " location - January 15th 010 midnight 54
Figure 73 : Wave directional spectrum obtained WWIII Norgas wave model - "Pierres Noires " location - January 15th 010 midnight.....55
Figure 74 : Wave spectra and second order Doppler spectra on ctober 14th 009 03:00 - "Les Pierres nNoires". Initial model (upper plot), final model after inversion (lower plot).....56
Figure 75 : Wave spectra and second order Doppler spectra on ctober 14th 009 03:00 - "Les Pierres Noires". Initial model (upper plot), final model after inversion (lower plot).....57
Figure 76 : mnidirectional spectra over the period ctober 009 - December 009, "Pierres Noires" wave buoy (left), modified empirical method (center), linearized inversion SeaView (right).....57
Figure 77 : Significant wave height over the period ctober 009 - December 009, "Pierres Noires" wave buoy, modified empirical method, linearized inversion SeaView. 58
Figure 78 : Significant wave height at the "Pierres Noires" location - comparison between linearized method and in-situ measured data 58
Figure 79 : Significant wave height at the "Pierres Noires" location - comparison between modified empirical method and in-situ measured data.....59

Figure 80 : Peak period over the period ctober 009 - December 009, "Pierres Noires" wave buoy, modified empirical method, linearized inversion SeaView 59
Figure 81 : Peak period at the "Pierres Noires" location - comparison between linearized method and in-situ measured data 60
Figure 8 : Peak period at the "Pierres Noires" location - comparison between modified empirical method and in-situ measured data 60
Figure 83 : number of valid Hs data per pixel 61
Figure 84 : Mean difference between raw data and filtered data.....6
Figure 85 : Mask based on two first criteria (red pixels are removed) (left). Average Hs for the year 010 (right) 6
Figure 86 : Final mask using the three criteria (red pixels are removed) (left). Resulting map for the mean Hs for the year 010. (right). 63
Figure 87 : Mean Hs from radar measurement (ctober 009 - June 011).....64
Figure 88 : Maximum Hs from radar measurement (ctober 009 - June 011) 64
Figure 89 : Hs monthly means for months January to June (ctober 009 - June 011).....65
Figure 90 : Hs monthly means for months July to December (ctober 009 - June 011)....66
Figure 91 : control points for the statistics.....67
Figure 9 : Histograms of Hs for the 5 control points 67
Figure 93 : Hs monthly statistics for the 5 control points 68
Figure 94: Percentage of valid data per pixel.....69
Figure 95: Mask based on data availability. n the red pixels data availability is less than 50 %, therefore these data have been removed for subsequent analyses. 70
Figure 96: Mean Hs measured by the radars at Pendeen and Perranporth (March 011 – September 01).....71
Figure 97: Maximum Hs measured by the radars at Pendeen and Perranporth (March 011 – September 01).....71
Figure 98: Hs monthly means for months January to June. 7
Figure 99: Hs monthly means for months July to December. 73
Figure 100: Control points for the statistics 74
Figure 101: Histograms of Hs for the 5 control points 74
Figure 10 : Hs monthly statistics for the 5 control points. 75

$.

G - H

IH I J @ B 00@

0 : % (.

= .

= 0 ! % ! $ ((

1"# $

= % K! $ (L K' $ (L

$

= 4 # . $ % .

= 5 2 ($

=)0 ((% (* + . $

2 - .

=)) @ . (. %

. % .

=)4 (%

' => ?

D (H 2) * 2)+

23# # ! % ($

(! $ (*!$+ .M

(! $ ((

Results are presented for the East-West, North-South components as well as for the total current. The period of comparison is limited to the month of September 005 with spring tides (coef>105) around the 19th of September and neap tides (coef<36) around the 6th of September.

%

Presented here are results related to the East-West current vector.

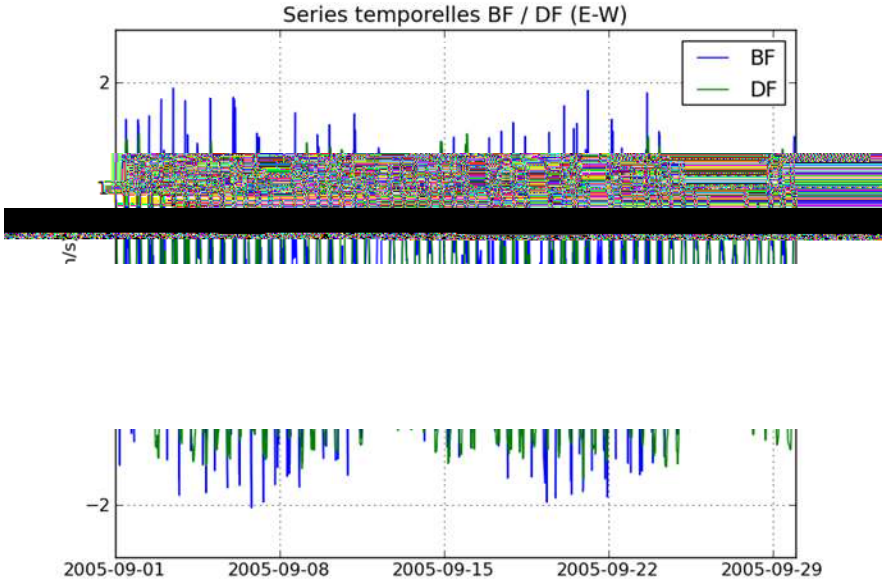

Figure 3 & /ime series for the " methods *F 1blue2 and DF 1green23 East%#est com'onent.

Correlation between two methods is 0.837608 and the RMS value is 0.519096 $m.s^{-1}$.

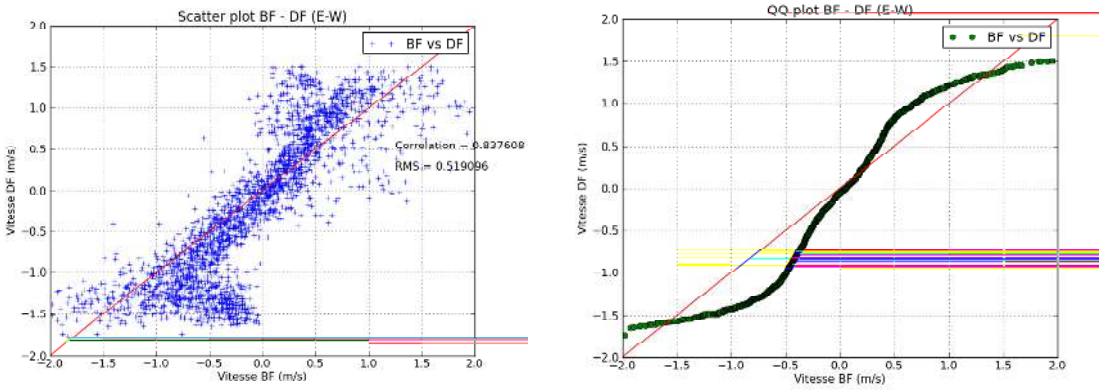

Figure ! & Scatter 'lot and 4%4 'lot for both methods *F and DF3 East%#est Com'onent

The bounding effect visible at the extremes of the scatter plot and Q-Q plot is due to the definition of a maximal authorized radial velocity in the Direction finding method.

& '

Presented here are results related to the North - South current vector.

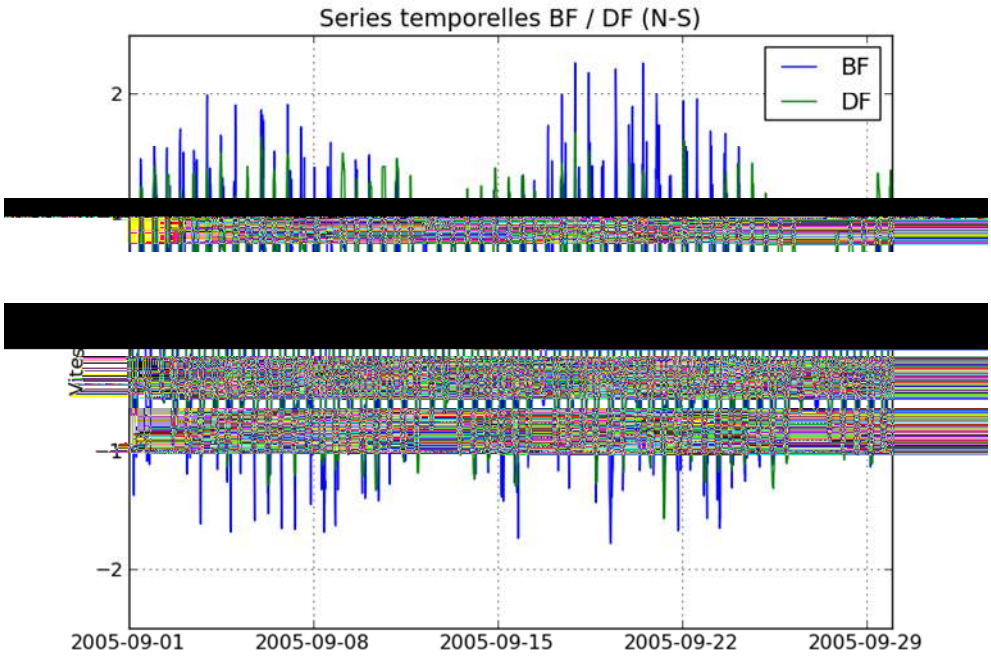

Figure (& /ime series for the " methods *F 1blue2 and DF 1green23 5orth % South com'onent.

Correlation between two methods is 0.906 11 and

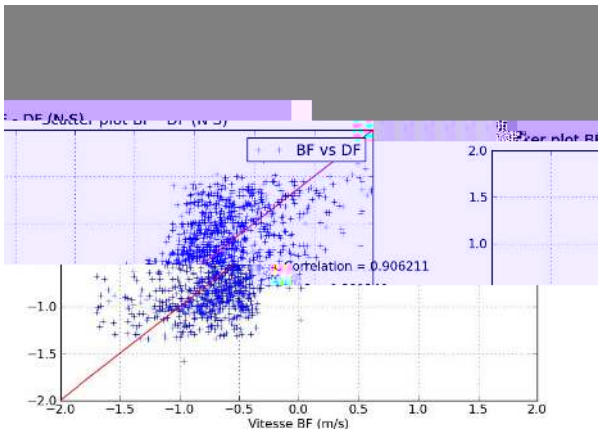

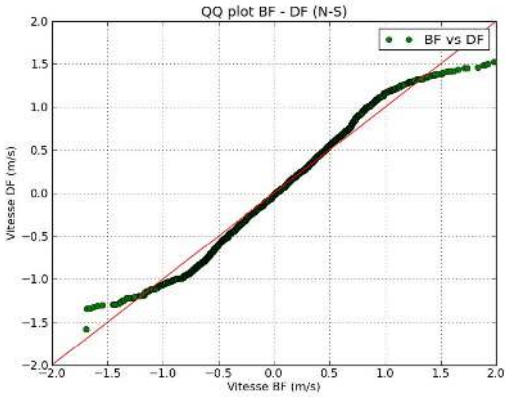

Figure - & Scatter 'lot and 4%4 'lot for both methods *F and DF3 5orth 6 South Com'onent

The bounding effect visible at the extremes of the scatter plot and Q-Q plot is due to the definition of a maximal authorized radial velocity in the Direction finding method.

(&)

Presented here are results related to the norm of the total vector of the measured current.

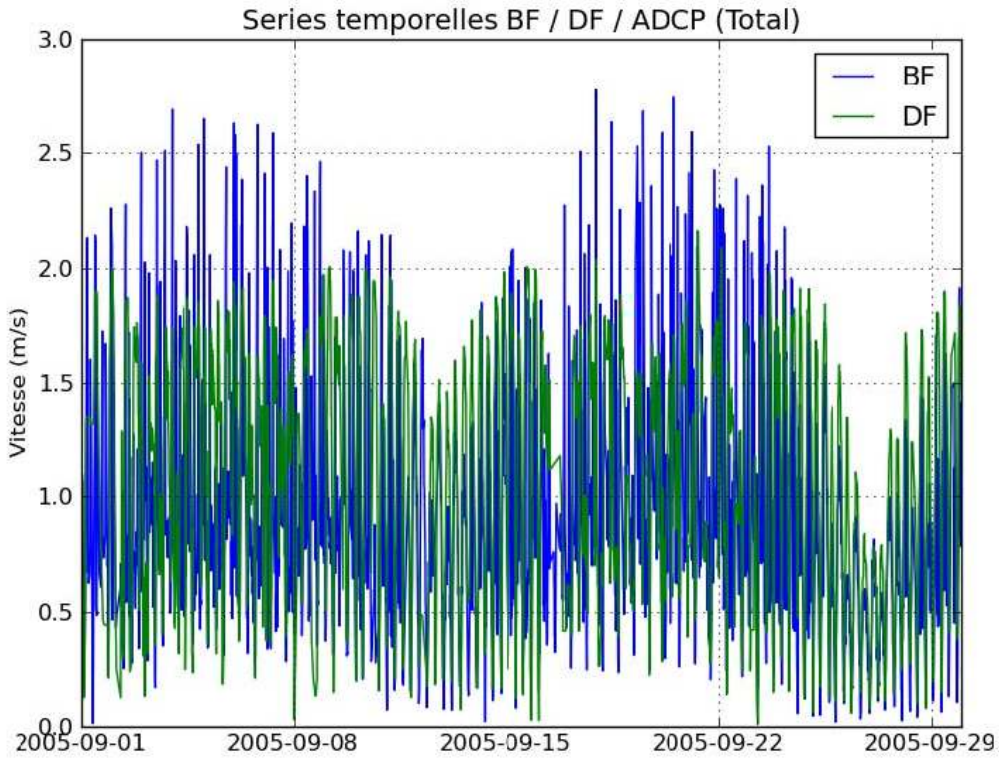

Figure , & /ime series for the " methods *F 1blue2 and DF 1green23 5orm of the total vector.

Corr

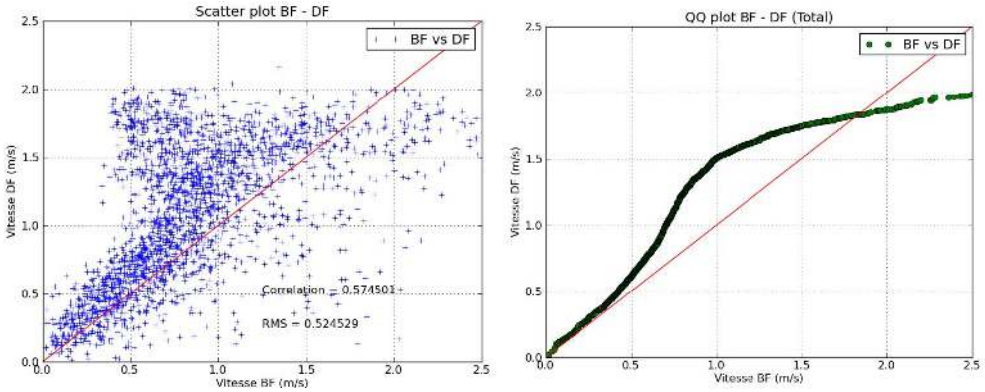

Figure 7 & Scatter 'lot and 4%4 'lot for both methods *F and DF3 5orm of the total vector

The bounding effect visible at the extremes of the scatter plot and Q-Q plot is due to the definition of a maximal authorized radial velocity in the Direction finding method.

* #

Comparison made on current velocities evaluated by the two methods BF and DF show a good correlation for low velocities (norm<0.5 m/s). Agreement is not so good for higher velocities.

ne reason for this is the difference in azimuthal resolution between the two methods. ver the considered area (Fromveur), the azimuthal resolution is of about 5° for the BF method and 1° for the DF method. This, combined with the local high current spatial gradients associated with the strong currents explains the differences observed between BF and DF for the strong currents.

(# $ +

Different sets of current measurement made by mean of ADCPs during various surveys conducted over the period 005- 011 were provided by Ifremer with the objective of validating the current velocities estimated from HF radar data using both DF and BF methods.

Locations of the ADCPs are shown figure Fig 10.

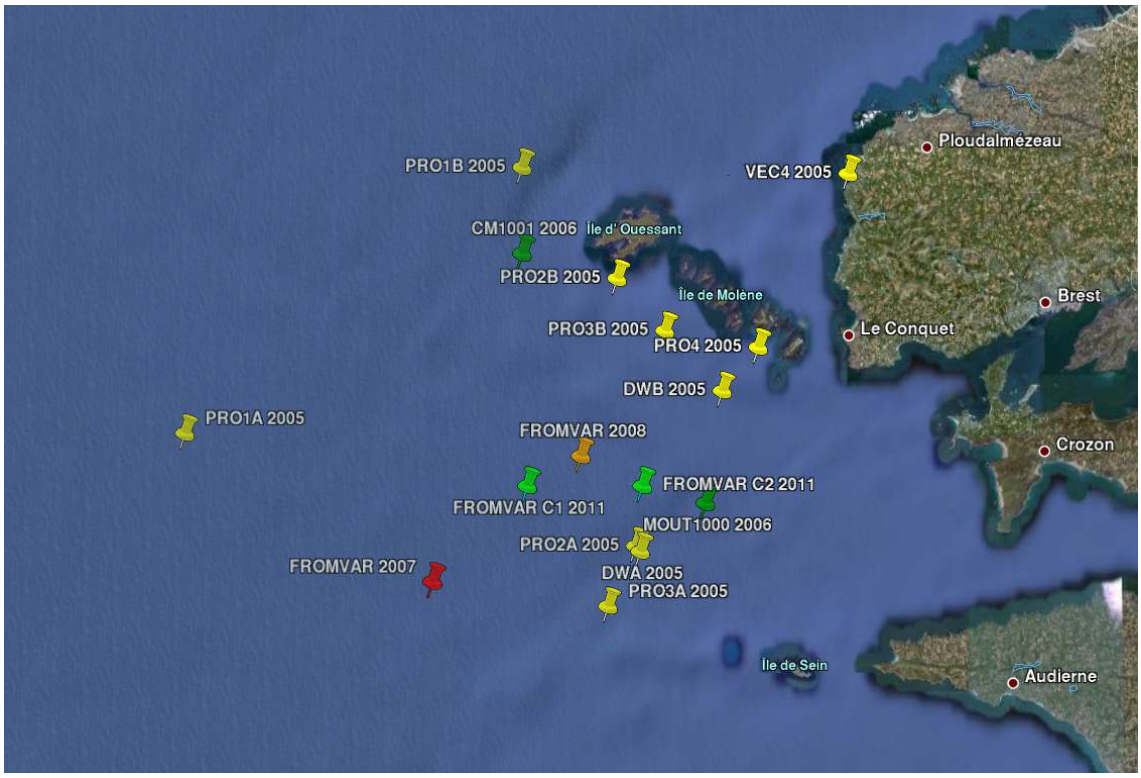

Figure 8 & ocation of the $DCP surveys over the Iroise Sea

We only present in this report the results of the comparisons between the BF and DF methods and ADCP surveys PR A (48.147 ° N, -5.1000°W) and PR B (48.40111°N, -5.1 1667° W) conducted during august and September 005. The area where the ADCP PR A was placed is characterized by currents globally more homogeneous in space and time than the currents observed in the area PR B which is much more dynamical. Location of ADCP PR B is also closer to the Fromveur area which is the area of interest for this project.

(#" "

Presented here are results related to the East-West current vector.

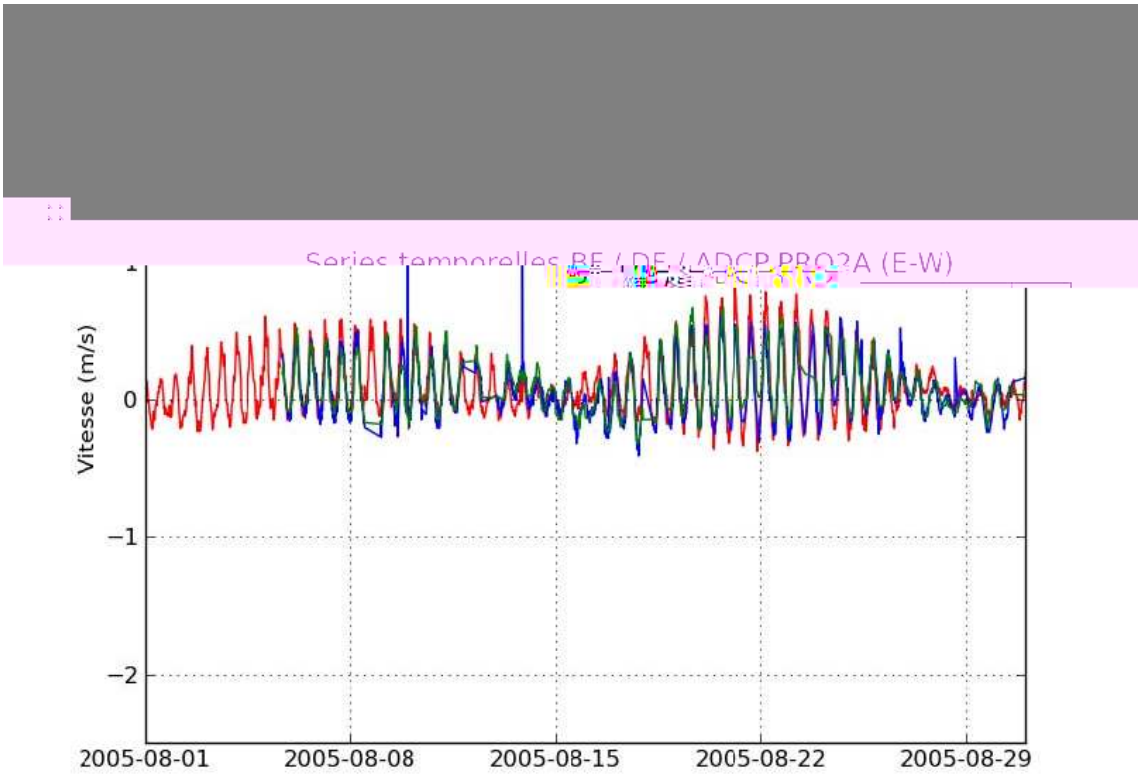

Figure 9 & /ime series of $DCP measured 1red2 and *F 1blue2 and DF 1green2 methods3 East%#est com'onent

Correlation between ADCP measurement and BF method is 0.8 8058 and the RMS value is 0.11986 $m.s^{-1}$.

Correlation between ADCP measurement and DF method is 0.830774 and the RMS value is 0.118608 $m.s^{-1}$.

Correlation between BF and DF methods is 0.906411 and the RMS value is 0.086757 $m.s^{-1}$.

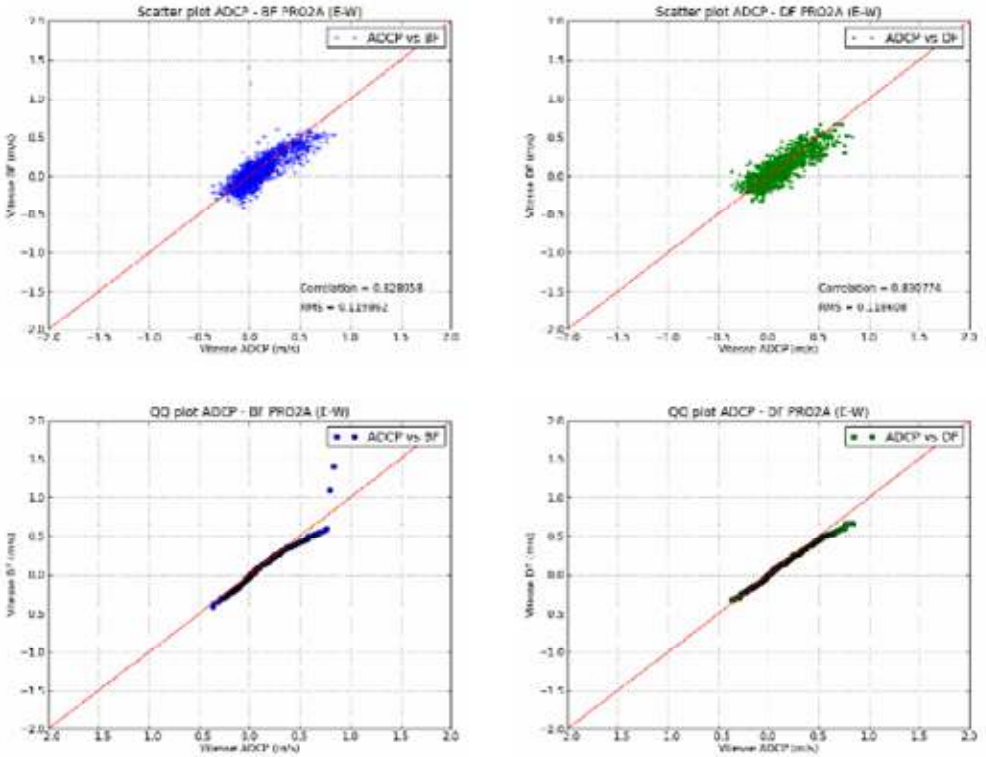

Figure & Scatter 'lot and 4%4 'lot for both methods *F 1blue2 and DF 1green2 as functions of $DCP measurement3 East%#est Com'onent

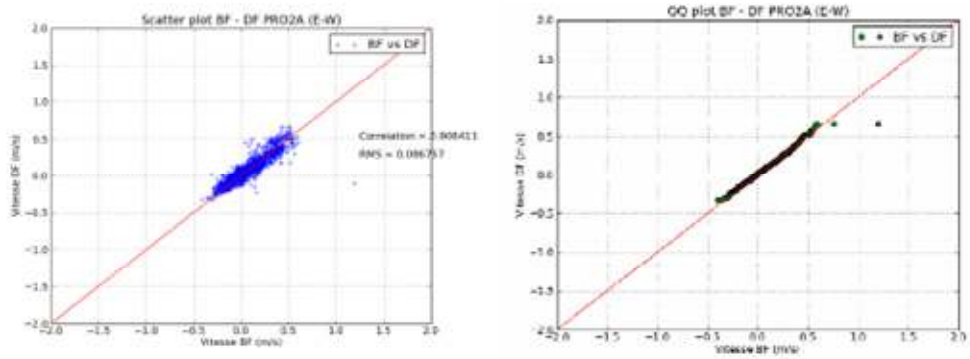

Figure "& Scatter 'lot and 4%4 'lot com'arison of *F and DF methods3 East%#est Com'onent

Presented here are results related to the North - South current vector.

Correlation between ADCP measurement and BF method is 0.918693 and the RMS value is 0.167188 $m.s^{-1}$.

Correlation between ADCP measurement and DF method is 0.874806 and the RMS value is 0. 04051 $m.s^{-1}$.

Correlation between BF and DF methods is 0.9 1519 and the RMS value is 0.158901 $m.s^{-1}$.

&/ $ 1 2 * 1 2 1 2 35 %
'

!& ' 4%4' * 1 2 1 2 $
35 % '

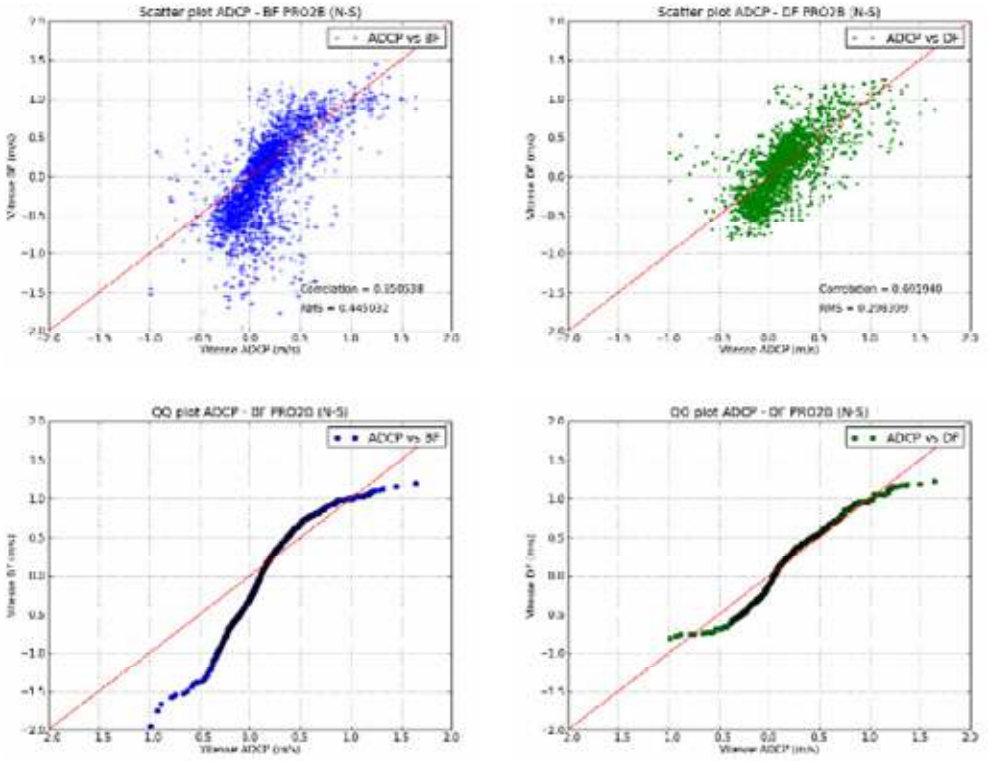

Figure "3 & Scatter 'lot and 4%4 'lot for both methods *F 1blue2 and DF 1green2 as functions of $DCP measurement3 5orth % South Com'onent

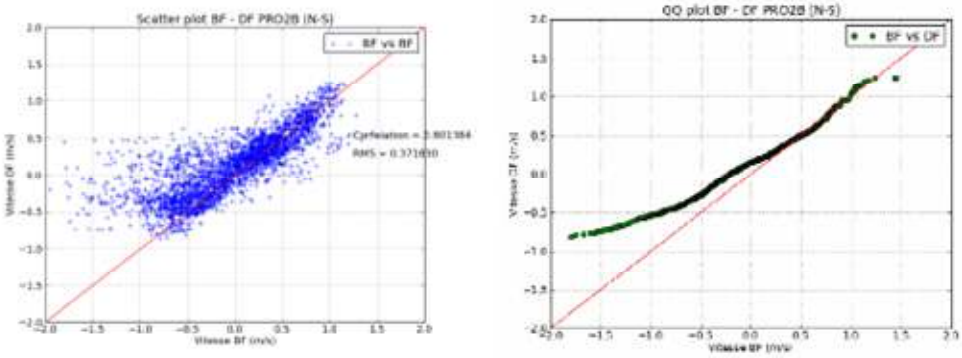

Figure "! & Scatter 'lot and 4%4 'lot com'arison of *F and DF methods3 5orth % South Com'onent

! "!

Presented here are results related to the norm of the total vector of the measured current.

Correlation between ADCP measurement and BF method is 0.386750 and the RMS value is 0.39 006 $m.s^{-1}$.

Correlation between ADCP measurement and DF method is 0.506309 and the RMS value is 0. 8 74 $m.s^{-1}$.

Correlation between BF and DF methods is 0.439643 and the RMS value is 0.344 09 $m.s^{-1}$.

"(&/ $ 1 2 * 1 2 1 2 3 5

"- & ' 4%4 ' * 1 2 1 2 $
3 5

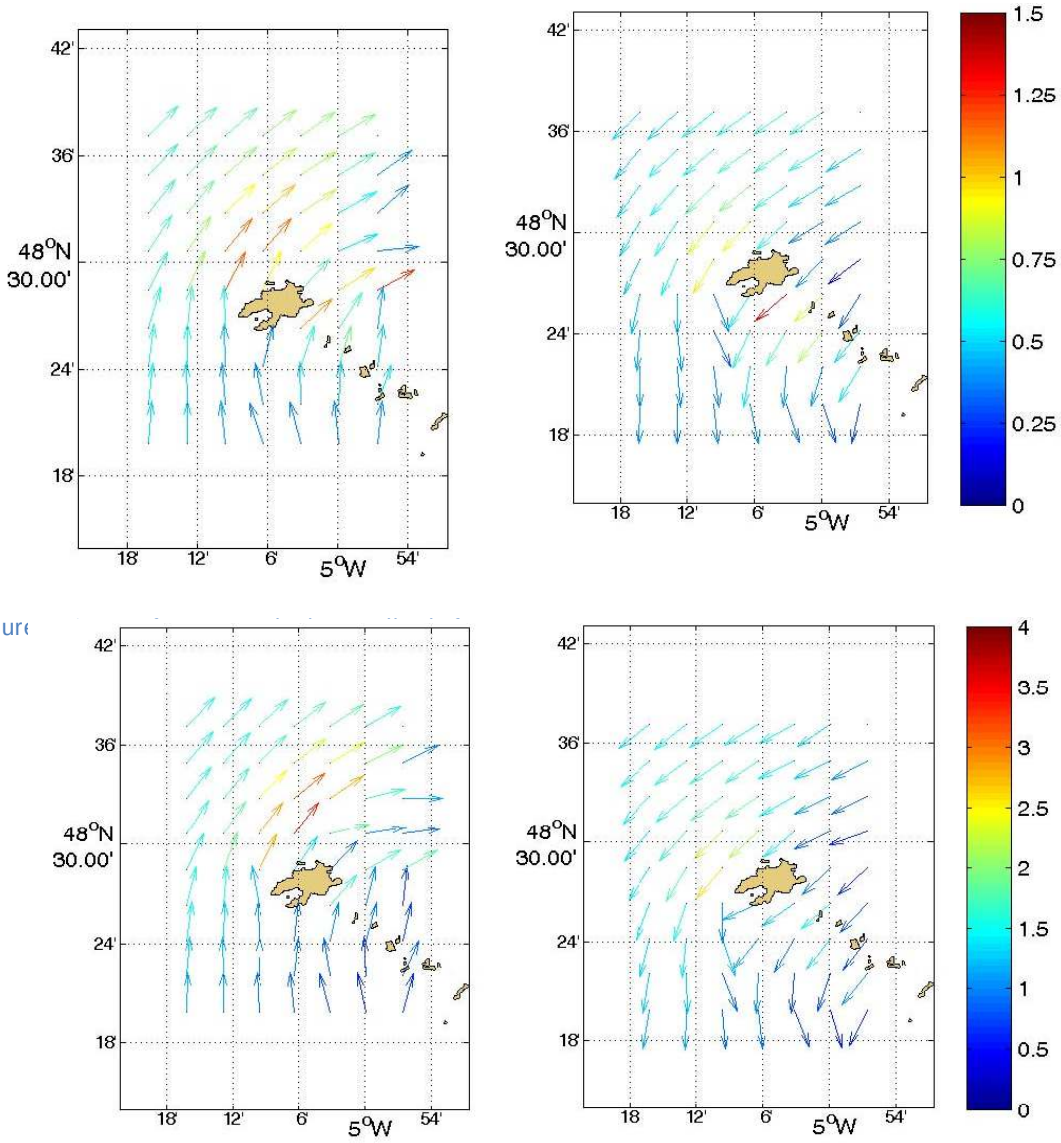

Figur(

Figure ! , & MaB of current velocity am ' litude for flood 1left2 and ebb 1right2 for a tidal coefficient of **8(**

In this chapter are presented comparisons of the beam forming (BF) and direction finding (DF) azimuthal methods based on analysis of previously assessed statistical indicators.

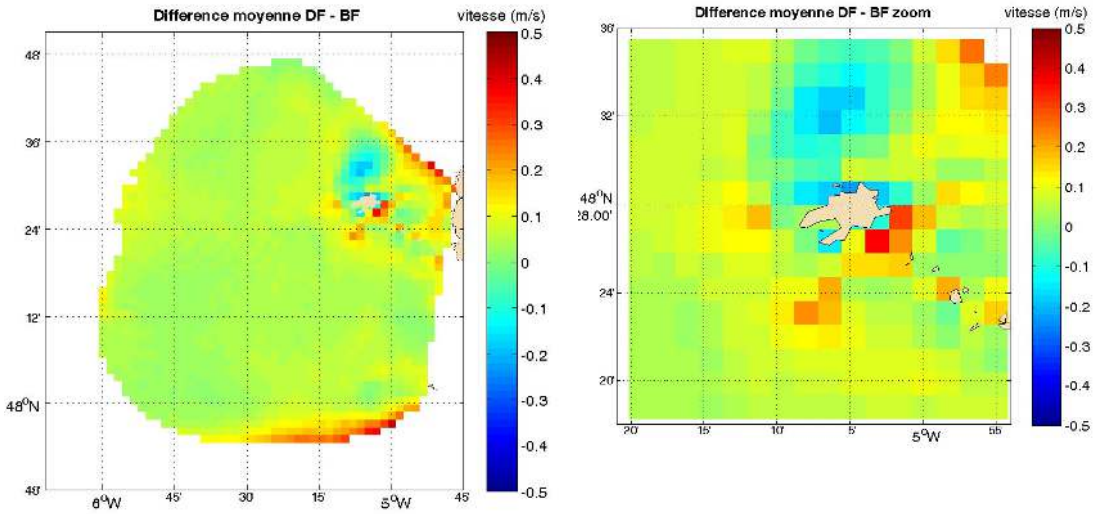

Figure !7& Ma's of the differences of the annual mean current velocity obtained using DF and *F methods

Maps of the annual differences between DF and BF methods presented on figure 48 show that globally, the DF method provides currents value slightly higher than those provided by the BF method. The wider differences are observed where the DF method provides higher values in the Fromveur strait and lower values in the north of Ushant island.

All the analyzed statistical indicators confirm that the DF method provides higher values, especially in the Fromveur strait (figures 49 and 50 hereafter). However, the trends observed for the c

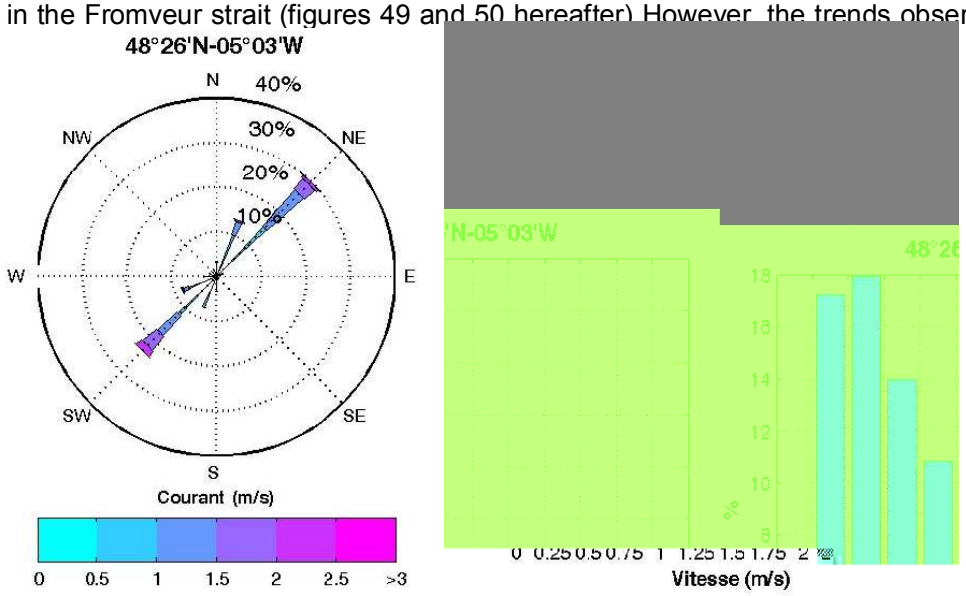

Figure !8& *F method3 statistics in the Fromveur strait 1'oint 5? 2& velocity com'ass and histogram.

(9 & 3 1' 5? 2 & '

The HF radar data is available with a 30 minutes time step. For this comparison the HF radar data are compared with the data corresponding to the closest date in the wave buoy time series.

Time series, scatter plots and Quantiles-Quantiles plots are presented Figure 5 for buoy 0 911 and Figure 53 for buoy 0 90 .

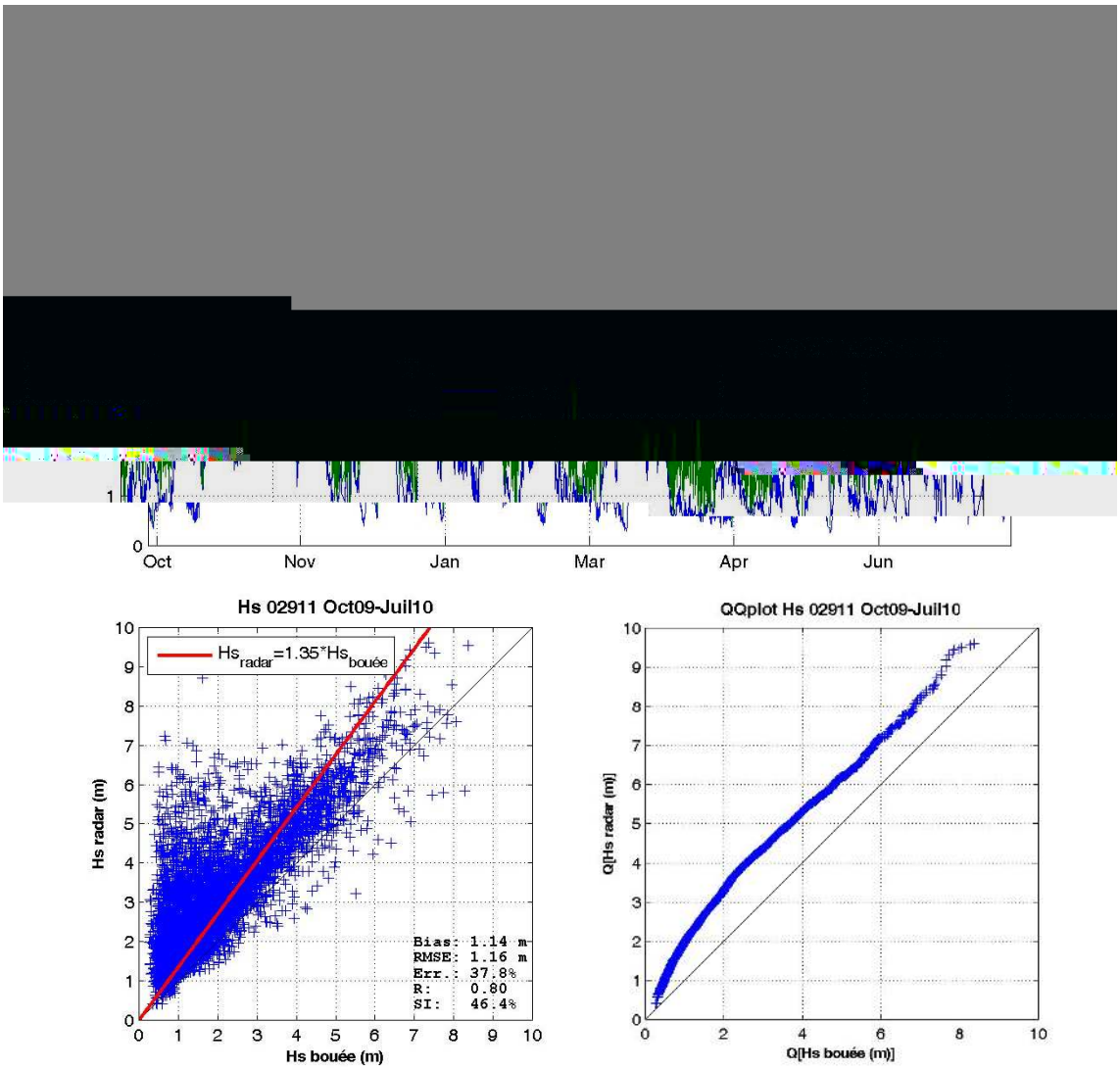

Figure ("& com'arison of HF radar and 9"8 =ave buoy Hs data% .ctober "998 to Culy "9 9.

Figure (3&com'arison of HF radar and 9"89" =ave buoy Hs data% .ctober "998 to Culy "9 9.

These results show a rather good correlation (>0.80) between wave buoys and HF radar Hs. However, a large bias (> 1 m) is observed, the HF radar overestimating the significant wave height.

The linear relation coefficient between the two data sets is estimated with a value between 1.35 and 1.6.

These results show that it i11W 8gsV,WWb5SgtVSb11W 8g V,83bS338gdV,t i11S3 SgeV,Sb11S46

’

. % = (

(! % (

(Q; ;6 , ; 6 R

1 ' ; :00 K L 3 . ;;: ,

! . ;;: % . # . % (

! % (

. . %

$ (65 . (%

. - ' H .

% * (+

.

(! & '

(- . (

; :00 % . ! . ;;:

1 . . . (66

1 . . (67

. . 06 % (

0 *; :6+ # 2 ; 6: * 0 05 +

eliminating possible erroneous measurements provided by the radars. This choice also

(7 & ' 9"89" = % . "998 C "9 9 %
'

. . ; :00 K L % (
. % % . $ % (. . %
;

% - . . ; :; K3 (L %
. ? . %

. % % . % 0 ;8
. ; :00 0 54 . ; :;

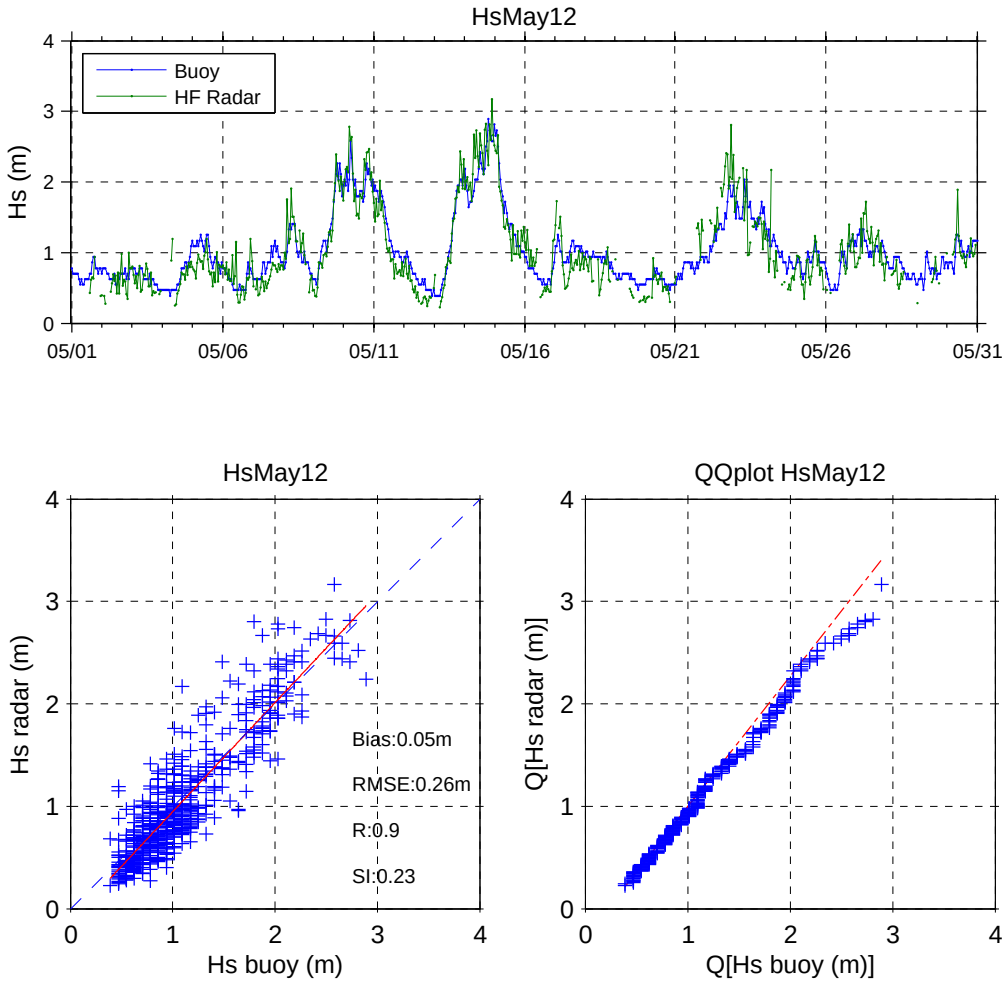

Figure , & Com'arison of HF radar and =ave buoy Hs data 6 May "9 " 6 Modified em'irical method.

The effect of applying an in-situ calibration for the Celtic Sea increases the correlation between buoy and radar measurements by 1% when compared to the results obtained with the classical empirical method. The error is reduced by 10% and the bias is cm lower. The calibration of the empirical algorithm is therefore beneficial not only for highly complex setups but also for simple radar configurations.

(* +)) , 45 6

-

The equations describing the interaction between the sea surface and the electromagnetic signal emitted by the radars in the HF band were established by D. E. Barrick . Using these equations, the first and second order of the Doppler HF spectrum can be described as function of oceanographic parameters such as the directional wave spectrum. Within the

D.E. Barrick First order theory and analysis of MF/HF/VHF scatter from sea. IEEE Trans. Antennas Propag., AP- 0, -10, 197 .

Doppler spectrum measured by the HF radar, the information that is relevant for the characterization of waves is part of the second order so that the directional wave spectra can be estimated using inversion methods for the equations describing the second order. The equation describing the second-order backscattering coefficient is non-linear relative to the wave directional spectrum. Hence two different approaches are available:

- Linearize the second-order equation and solve the linear system
- Solve the non-linear equation

The linearized approach is the one adopted by L. R. Wyatt[3] and implemented in the commercial software SeaView. This method is also used for processing the HF radar data from the Iroise Sea.

The only existing method for the assessment of the wave directional spectrum without linearization of the equation describing the second order is the one proposed by Y. Hisaki[4].

This method consists of computing the second order equation for the HF radar configuration. Therefore, the directional wave spectrum is discretized, the points of the directional spectrum necessary for the assessment of the energy of the backscattered signal are saved and a non-linear inversion method such as Gauss-Newton or Marquart is finally used. As this nonlinear problem is ill-conditioned, it is necessary to impose constraints to the solution.

Figure ," & #ave directional s'ectrum obtained from nonlinear inversion of the radar data % DPierres

! , $ 1 2

The nonlinear inversion method for the Barrick equation based on Hisaki formulation was implemented and used for the processing of the Iroise Sea HF radar data. Various wave parameters can be derived from the directional spectrum. For instance, from the spectrum assessed at the location “Les Pierres Noires” on January 15th 010 at midnight (Figure 67), the derived Hs is .51 m, the peak period is 11.6 s and the peak direction is about 70°.

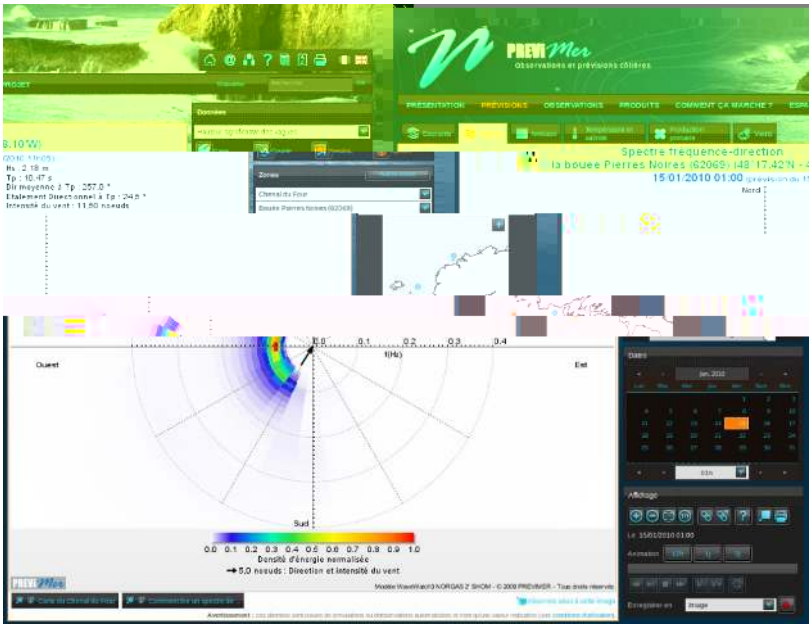

Figure ,3& #ave directional s'ectrum obtained # #III 5orgas =ave model %DPierres 5oires D location % Canuary (th "9 9 midnight

For validation purpose, these results are compared with the parameters obtained from the WWIII Norgas wave model at the same location and same date. Values provided by the model are Hs = .18 m, peak period 11.47 s, and peak direction 60° (Figure 68).

Results of numerous applications of this inversion procedure confirm that it is possible to assess the wave directional spectrum and the derived parameters using a non-linear inversion method. However, these results also confirm that this is not an easy problem to solve. The estimation of the wave directional spectrum from the Doppler spectrum is an ill-conditioned non-linear problem. The solution obtained after inversion also depends on the model initially used and several wave directional spectra can be obtained from one single input data set. The problem is depicted in Figures 69 and 70 : from two different initial directional spectra, the inversion algorithm converges towards two different directional spectra which describe in a similar way the input data but with a different physical meaning.

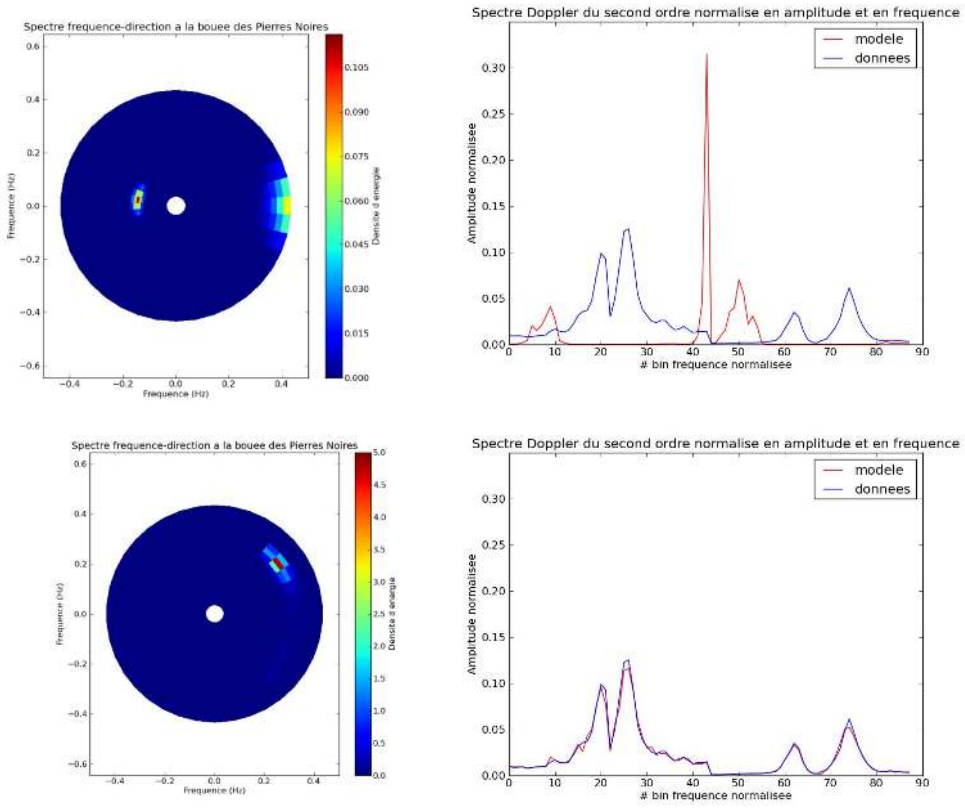

Figure ,! & #ave s'ectra and second order Do''ler s'ectra on .ctober !th "998 93&99 %D es Pierres n5oiresD. Initial model 1u''er 'lot23 final model after inversion 1lo=er 'lot2

So far, the non-linear inversion algorithm based on Hisaki formulation is providing good results from a mathematical or theoretical point of view but all results do not necessarily have a correct physical meaning. It can be envisaged for improvement of the quality of the inversion process to add information, whether it is a priori (for instance in the Iroise Sea there is often westerly swell) or a constraint like, for instance, wind intensity and direction.

$ $ $

As the results obtained using the non-linear inversion method are not quite satisfactory, we focus here on the comparison of results using the linearized inversion method (SeaView) and the modified empirical method presented in the previous chapters. This comparison is made using data assessed at the “Pierres Noires” location over the period ctober 009 – December 009.

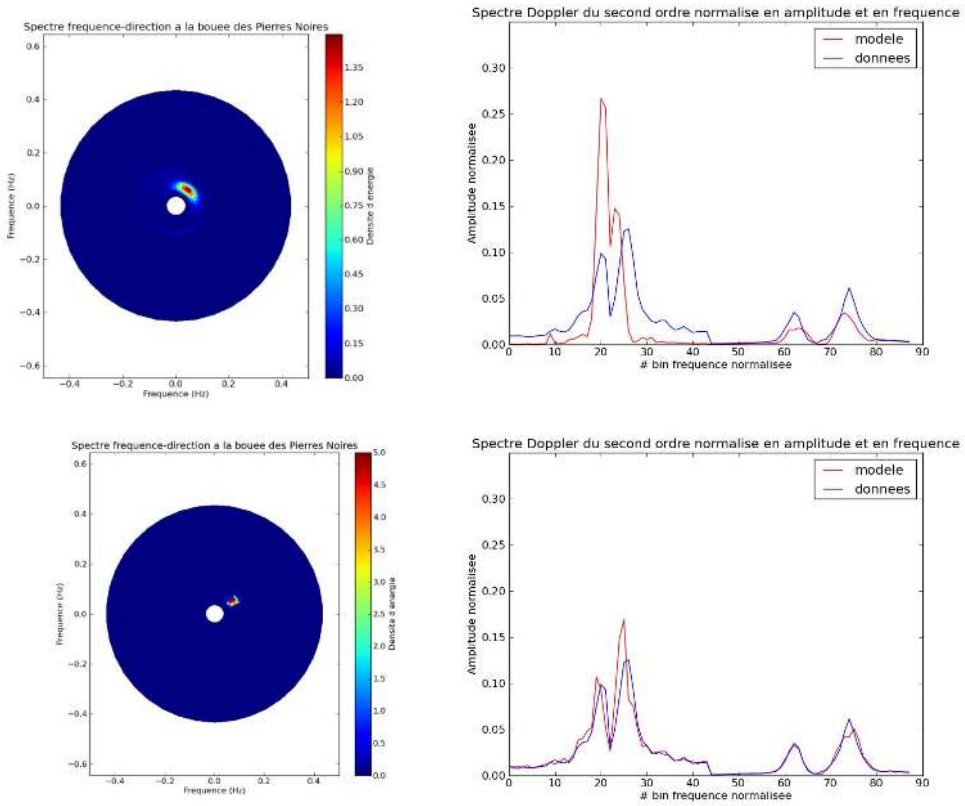

Figure , (& #ave s'ectra and second order Do''ler s'ectra on .ctober !th "998 93&99 % D es Pierres 5oiresD. Initial model 1u''er 'lot23 final model after inversion 1lo=er 'lot2

For this comparison, the omnidirectional wave spectra were computed (Figure 71). Hs was derived from these spectra (Figure 7).

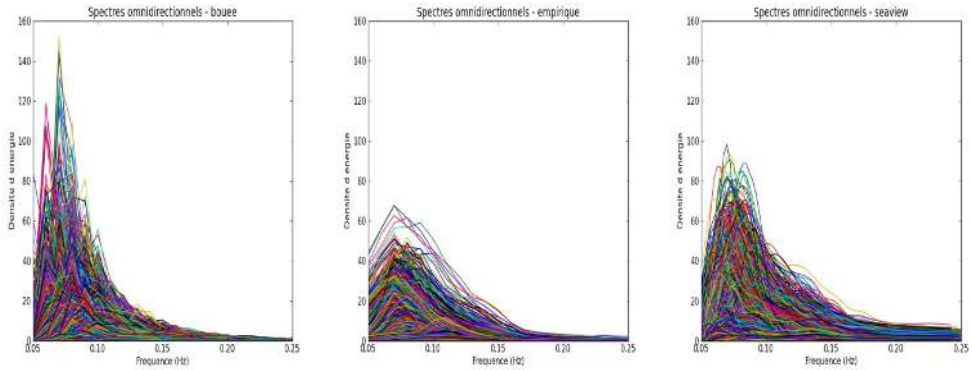

Figure , - & .mnidirectional s'ectra over the 'eriod .ctober "998 % December "998 3 DPierres 5oiresD =ave buoy 1left23 modified em'irical method 1center23 lineari0ed inversion Sea@ie= 1right2.

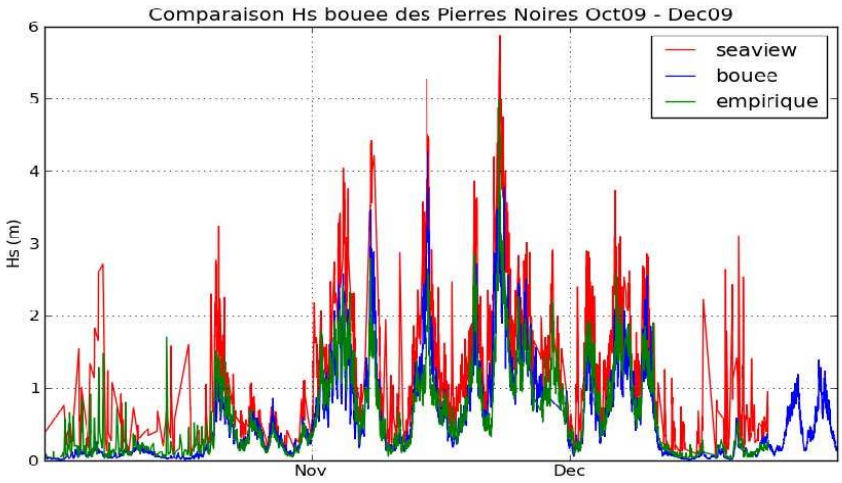

Figure , , & Significant =ave height over the 'eriod .ctober "998 % December "998 DPierres 5oiresD =ave buoy3 modified em'irical method3 linear0ed inversion S

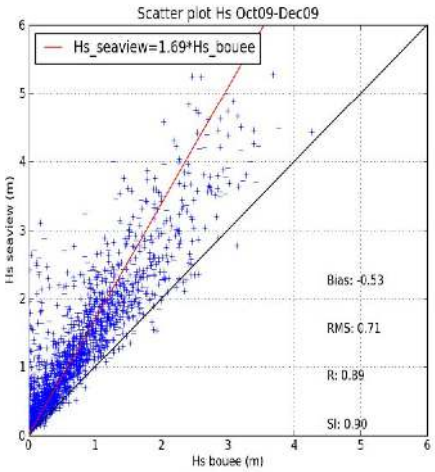

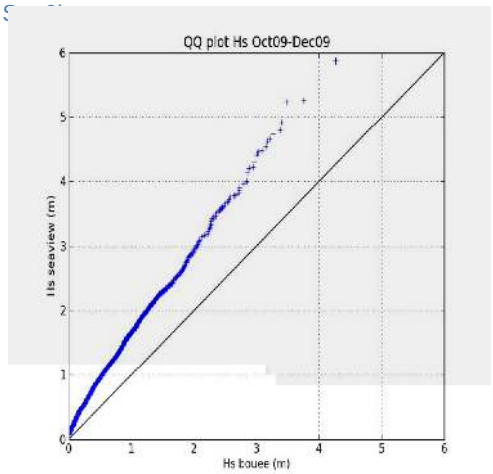

Figure ,7 & Significant =ave height at the DPierres 5oiresD location % com'arison bet=een linear0ed method and in%situ measured data

Hs derived from the adapted empirical method are in rather good agreement with the wave buoy data. Hs assessed using the linearized inversion method show a bias of about 50 cm, an RMS error of about 30 cm and a linear coefficient of 1.69. The agreement is not as good.

Peak period can also be derived from the omnidirectional spectra and are plotted Figure 75.

The distribution of the data observed in the scatter plots and Q-Q plot is due to the frequency sampling.

Results provided by the two methods cannot be considered satisfactory even if the modified empirical method provides a better estimate of the peak periods especially for the longer periods.

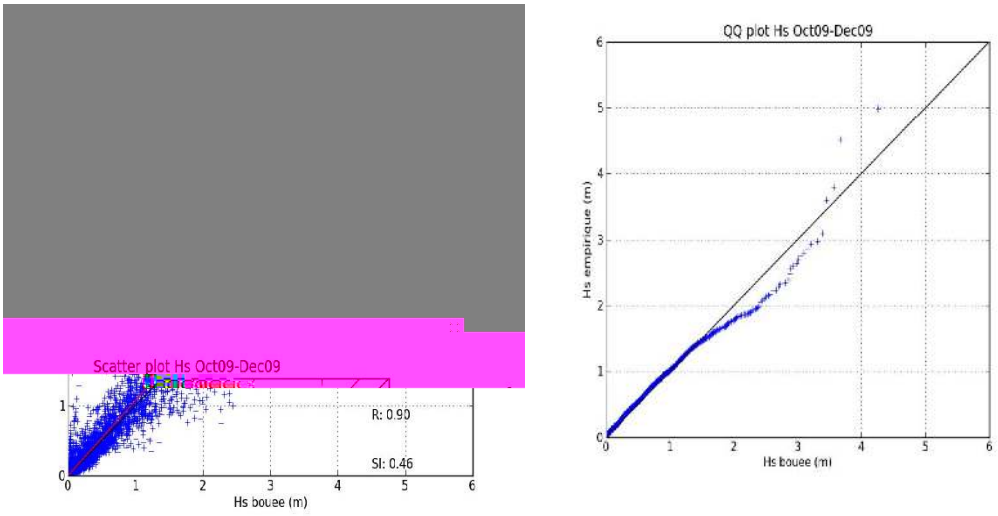

Figure ,8 & Significant =ave height at the DPierres 5oiresD location % com'arison bet=een modified em'irical method and in%situ measured data

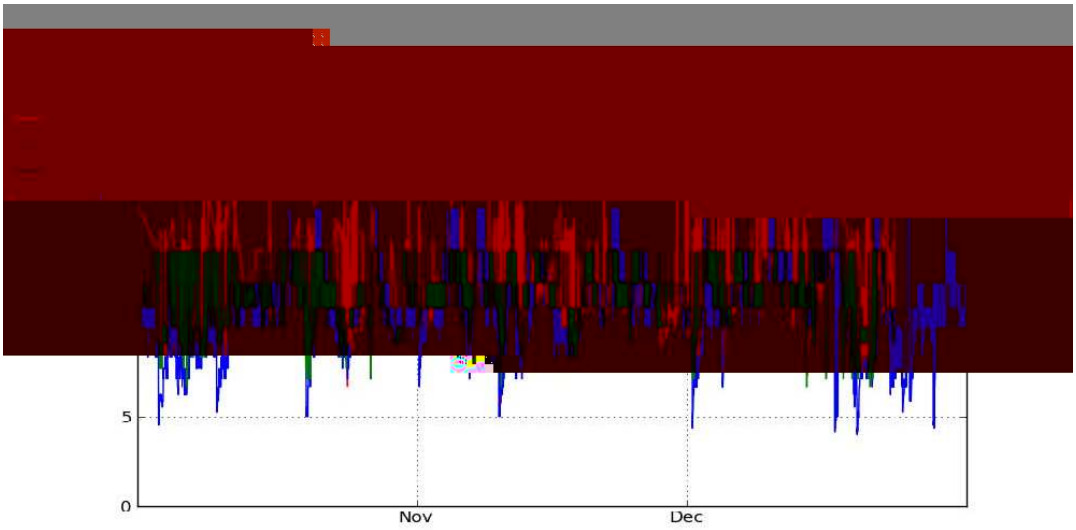

Figure 79 & Pea+ 'eriod over the 'eriod .ctober "998 % December "998 DPierres 5oiresD =ave buoy modified em'irical method linear0ed inversion Sea@ie=

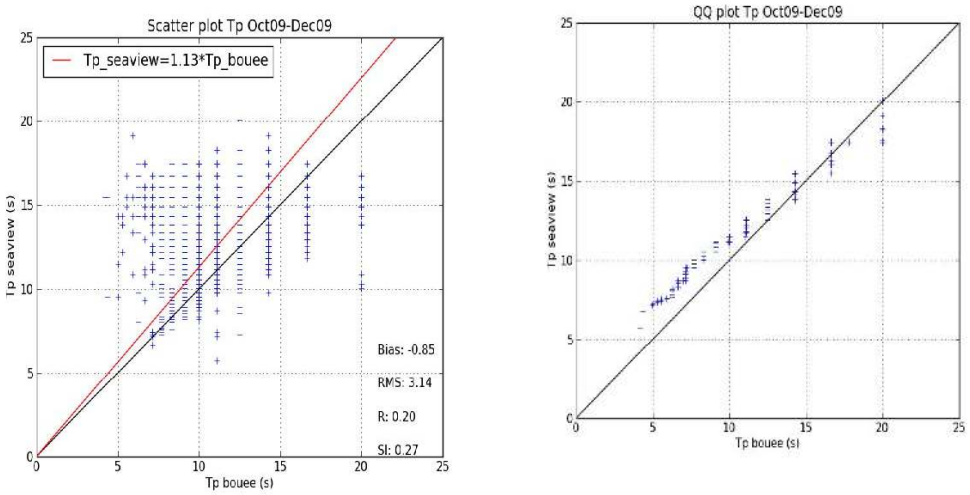

Figure 7 : Peak period at the Pierres Noires location : comparison between linearized method and in-situ measured data

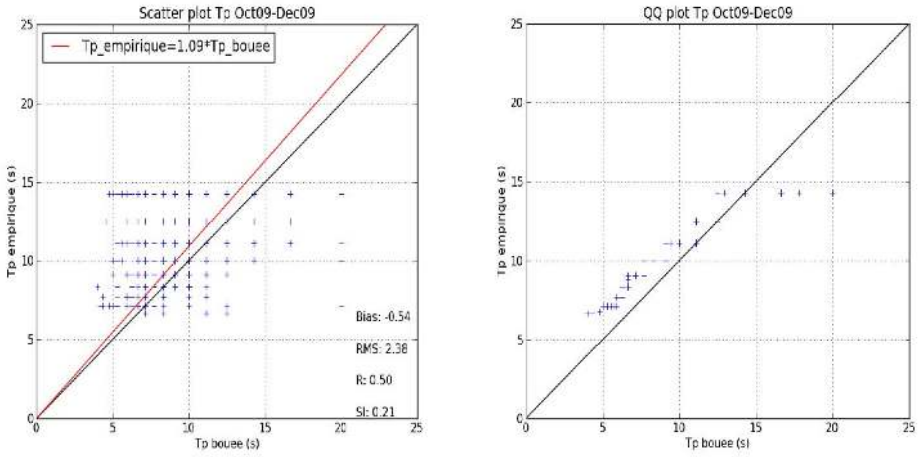

Figure 8 : Peak period at the Pierres Noires location : comparison between modified empirical method and in-situ measured data

($ +)

Results presented in this chapter were obtained from processing of the HF radars data using the modified empirical method.

('

1+ $ $

The covered geographical area is comprised between 47° 0' N and 49° 0' N in latitude and -06°45' W and -04°30' W in longitude. Statistics were built using data sets covering the period from October 2009 to June 2011 with a 30 minutes time step (638 days corresponding to 306 4 time steps).

Presented on the map figure 78 are the numbers of valid Hs data per pixel. The maximum number of valid values per pixel is 941. Among the pixels having data 13% cover slightly less than the total assessment period (about 10000 data per pixel) and only .4 % cover /3 of the time (> 0000 data per pixels)

Parameter	Number of pixels with N>0	Number of pixels with N>10000	Number of pixels with N>15000	Number of pixels with N> 0000
Hs	4 57 (100 %)	577 (13.6 %)	307 (7. %)	10 (.4 %)

/able & 5umbers of data 'er 'iBels on the 9E79 radar grid

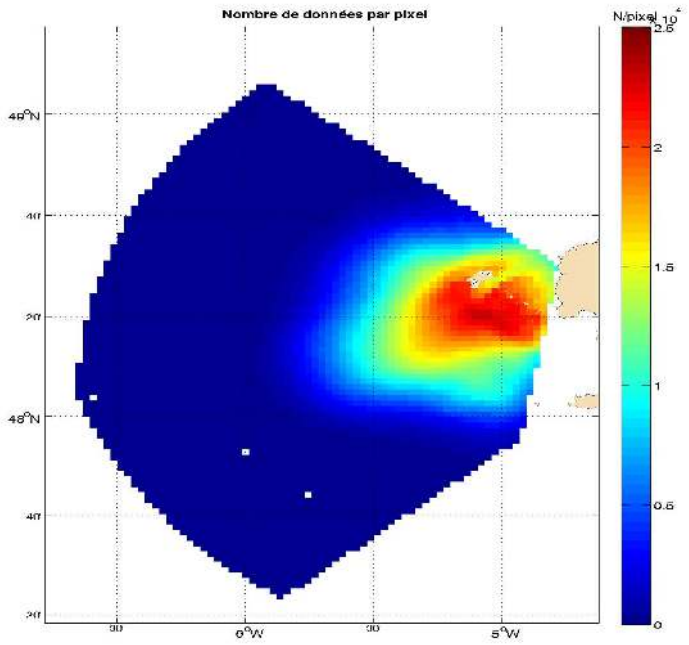

Figure 73 & number of valid Hs data 'er 'iBel

2

The algorithm used for the processing is sensitive to the noise in the radar signal, especially in the areas at the limit of the radar range and in the vicinity of the islands. As a consequence, a mask is built so as to improve the quality of the statistics. Three criteria are selected to build the mask and eliminate the data with the most noise :

- Pixels with a number of available data is lower than 15000 (50%)
- Grid points with strong space/time current gradient
- Pixels where the mean Hs value over the year 010 is larger than 3.5 m are removed.

The reason for the second criteria is that strong current gradients induce a spreading of the first order Bragg rays that will make difficult the identification and segmentation of the second order components of the Doppler spectrum. When this is the case, the Hs is often overestimated. The masked areas are then defined by comparison of the raw Hs value and data filtered using a moving average filter (over a half tidal cycle, about 6 hours). Areas

where the mean difference between the raw data and the filtered data is too high (>0.7) are masked (figure 79).

The mask based on the two first criteria is presented figure 80. Even when applying these two criteria, high values of the average significant wave height (about 3.5 m) can still be observed in some areas at the limit of the range or in the shadowed area behind Ushant island. In order to compensate for this, the 3rd criterion is applied.

The global mask is presented figure 81. After such processing only 5.9 % of the pixels are saved for the statistical analysis.

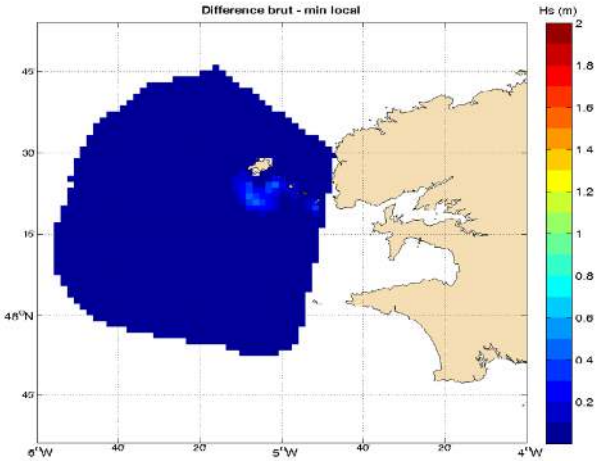

Figure 7!

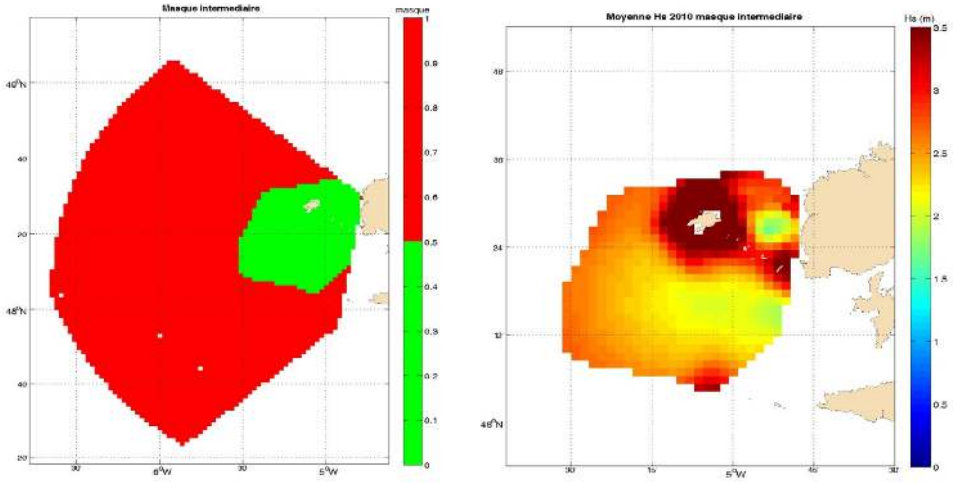

Figure 7(& Mas+ based on t=o first criteria 1red 'iBels are removed2 1 left2. $verage Hs for the year "9 9 1right2

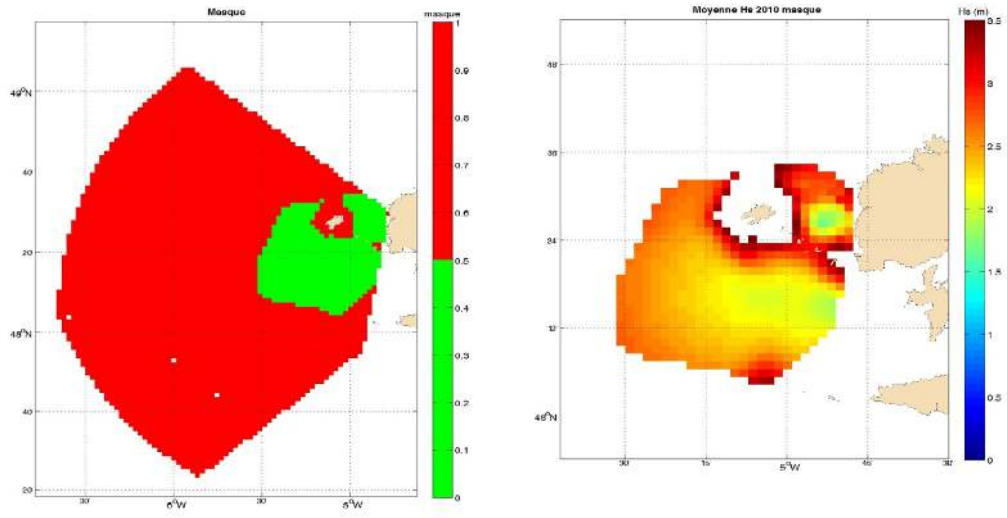

Figure 7- & Final mas+ using the three criteria 1red 'iBels are removed2 1left2. Resulting ma' for the mean Hs for the year "9 9. 1right2.

('

Mean Hs assessed from radar measurement for the whole period from ctober 009 to June 011 is presented figure 8 while the maximum Hs over that same period are presented figure 83.

ver the covered area the mean Hs in the west of the 5°W longitude is about .5 m it reduces to about m when getting closer to the coast.

The maximum measured Hs is almost uniformly 10 m over the area except between the islands and the mainland (These results should be used with caution as the modified empirical method sometime provides overestimated Hs values that will affect the statistics)..

Monthly mean values are presented figures 84 and 85. The mean Hs value during the period from ctober to March is of about .5 m over most of the area but a high variability can be observed especially comparing November and January.

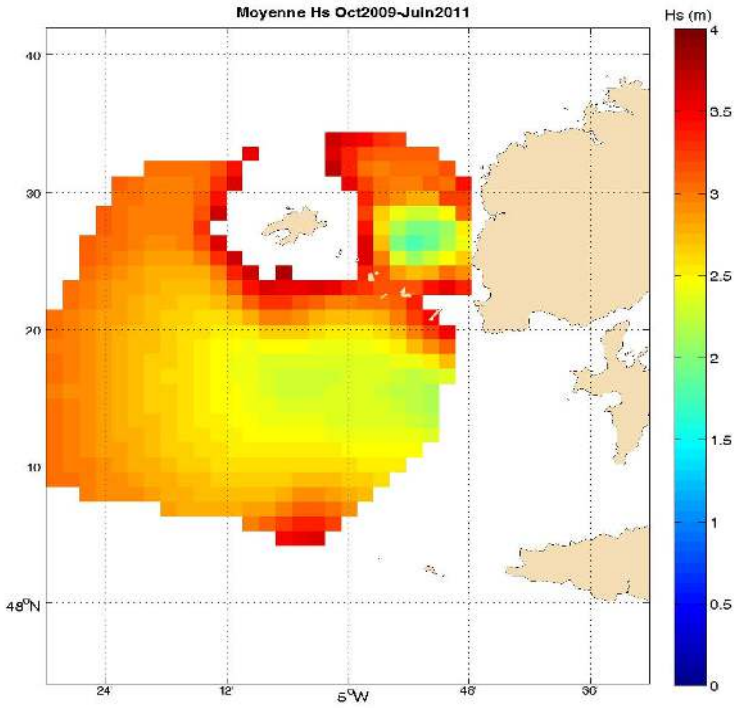

Figure 7, & Mean Hs

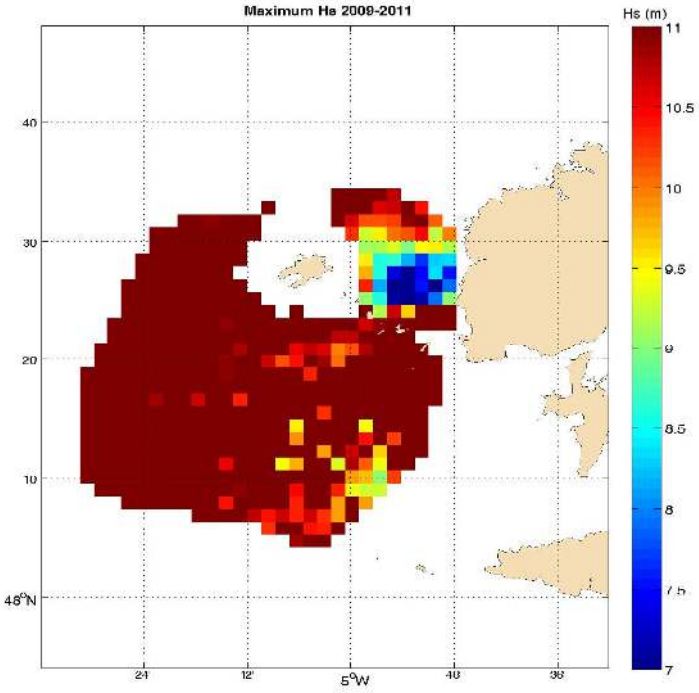

Figure 77 & MaBimum Hs from radar measurement 1 . ctober "998 % Cune "9 2

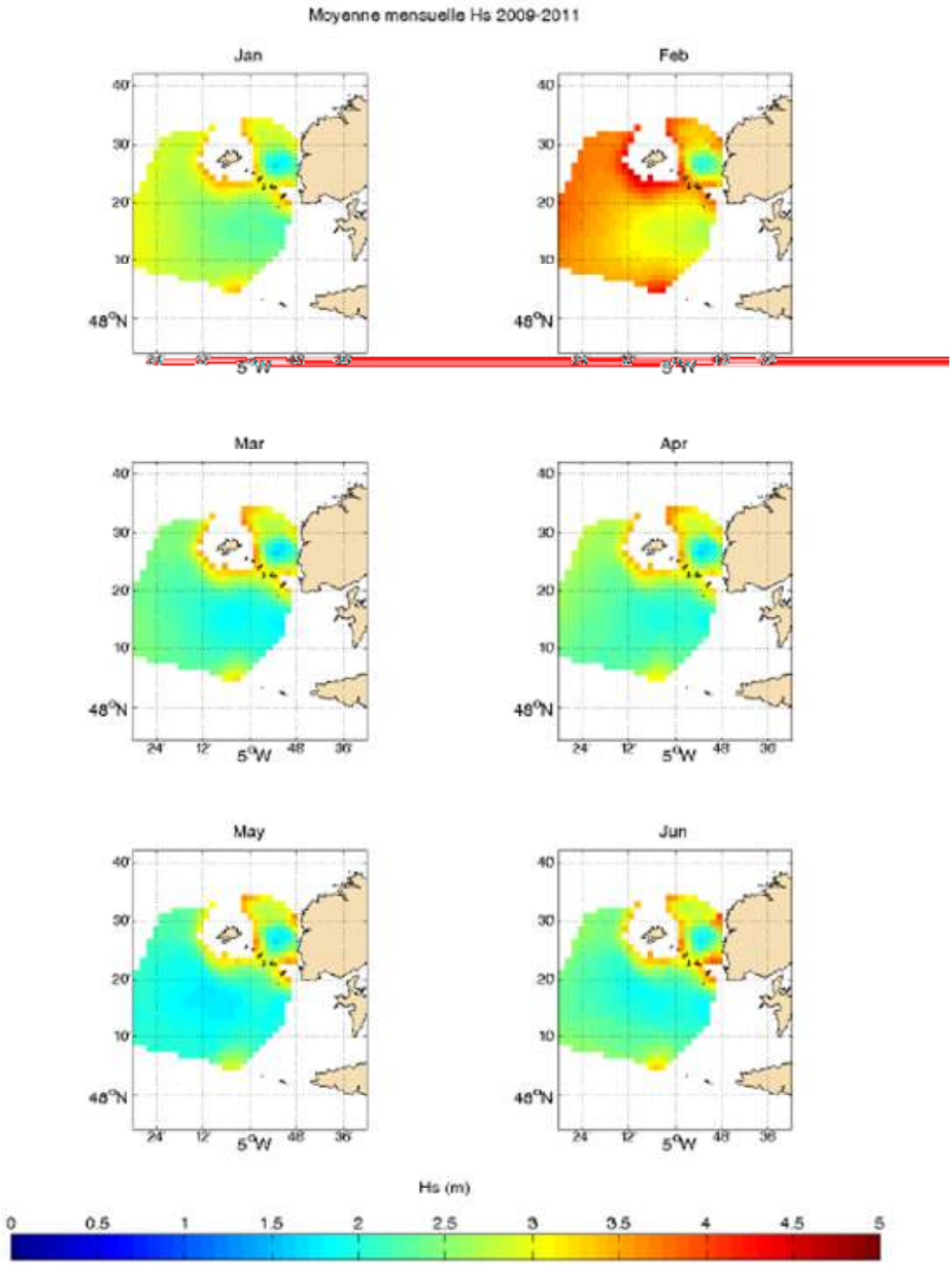

Figure 78 : Hs monthly means for months January to June 1998 to June 2012

89 & C 1 . "998 % C "9 2

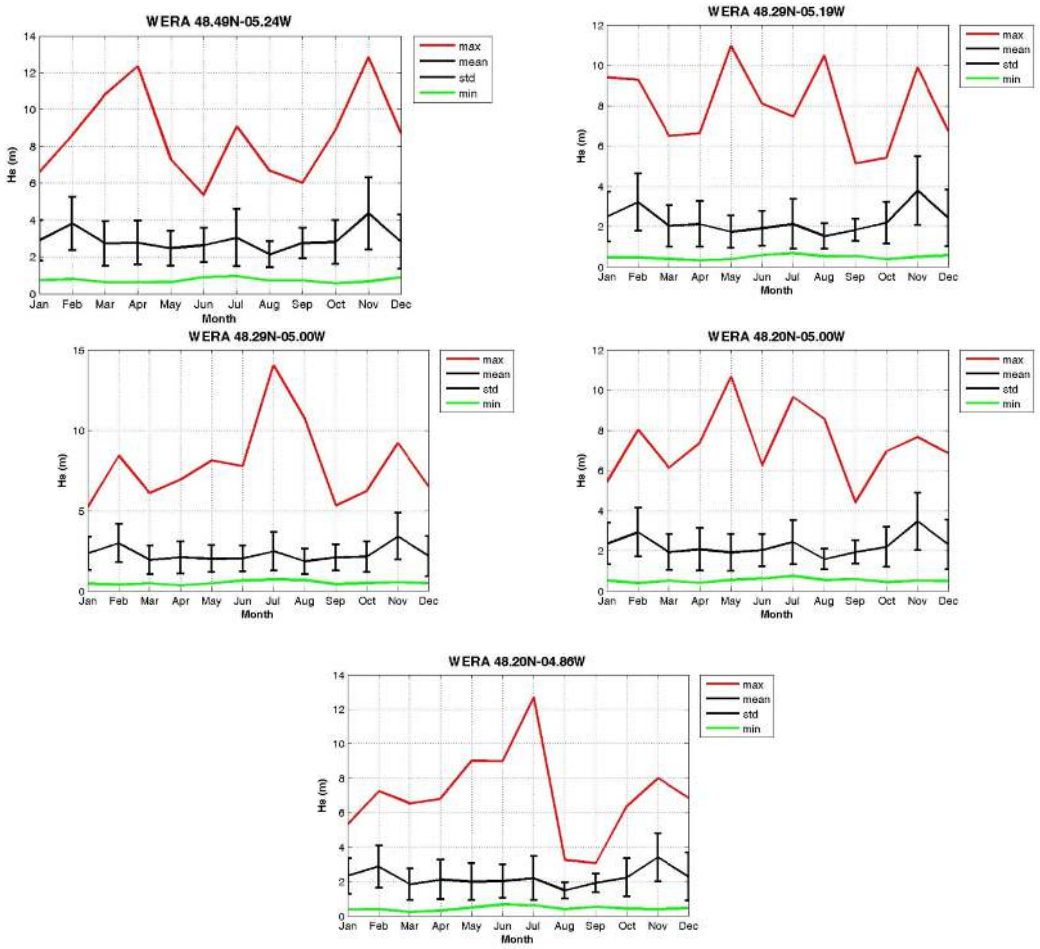

Figure 83 & Hs monthly statistics for the (control ' oints

(($ +) #

(('

1+ $ $

The radar system described in section 3.1. .4 operates at a centre frequency of 1 MHz, and makes independent measurements for 17 minutes every hour. These measurements are then used to generate maps of Hs on a 75-by-90 grid at a 1 km resolution. This measuring grid covers an area covering 50°1 .94' N to 51°1'N in latitude and between 05°5.03'W and 06°8'W in longitude. The dataset used to calculate the statistics presented in this section corresponds to 19 months' worth of data, from March 011 to September 01 , a period equivalent to 580 days and 13,9 0 time steps.

Depicted in Figure 94 is the percentage of the time each pixel in the grid has valid data. The maximum number of valid values is 11,4 8, which is 49 time steps less than the total.

0975 D 6;A 055; D
9;A

/ "& 5 ' ' B 89B,(

	. D % C;	. D % C6805	. D % C9680
	7604 *:7 5:A+	0975 * 8 7A+	055; * 0 44A+

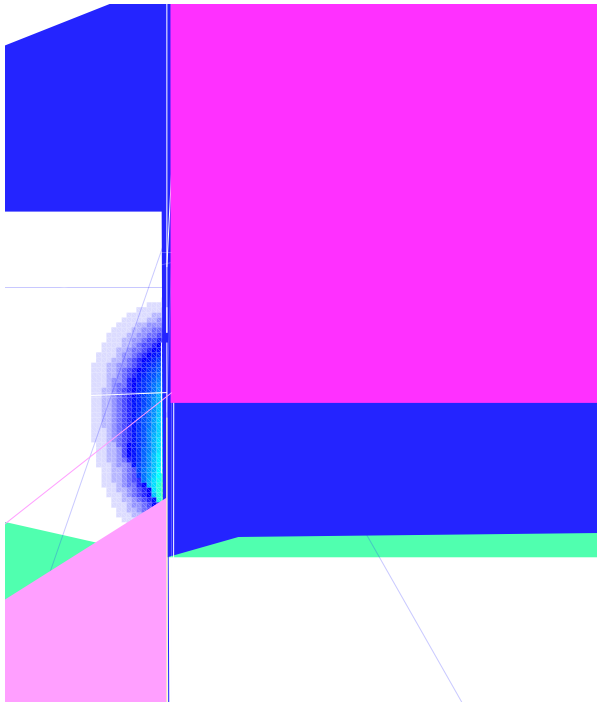

8!& ' ' B

2

4 0 - ((
((((
- % ((%
. D . !
- % M ((%
D % - .
. - D %
. 8;A . . ? *$ (:6+